nature communications

Article

https://doi.org/10.1038/s41467-026-69986-w

Experimental observation of non-Hermitian phase transitions using laser-induced thermoacoustics

Received: 29 September 2024

Accepted: 16 February 2026

Haixiao Zhang[1,2,6], Renhao Fan[1,3,6], Wei Xiong[1], Kefan Sun[1], Anxin Zhang[1,3], Zhiwang Zhang[1], Chen Shao[1], Chengrong Ma[1], Yechao Bai[4], Ying Cheng[1] ✉, Ruwen Peng[1,3] ✉, Xiaojun Liu[1] ✉ & Johan Christensen[5] ✉

Non-Hermitian physics in open systems has garnered significant attention for its exotic phenomena, particularly surrounding exceptional points that offer transformative potential for multifunctional devices. Central to this field are parity-time ($\mathcal{PT}$) symmetry-defined by balanced gain and loss-and its counterpart, anti-$\mathcal{PT}$ symmetry. However, integrating these divergent concepts into a unified acoustic platform remains an unattainable challenge. In this study, we employ laser-induced thermoacoustics (LIT) to integrate a tunable amplifying component into a non-Hermitian system. By exciting an ultrathin carbon nanotube (CNT) film through laser irradiation, we experimentally observe the phase transitions between $\mathcal{PT}$ and anti-$\mathcal{PT}$ symmetries. Furthermore, our findings demonstrate the creation of selectable scattering states and the generation of acoustic vortex beams (VBs), facilitating both $\mathcal{PT}$-symmetric scattering and the conversion of topological charges. This acoustically transparent strategy bypasses traditional, path-blocking compensation schemes, offering a versatile framework for controlled non-Hermitian phase transitions in next-generation integrated devices.

One of the most intriguing advancements in quantum mechanics over recent decades has been the discovery of non-Hermitian Hamiltonian H that commutes with the parity-time ($\mathcal{PT}$) operator, leading to the emergence of real-energy eigenvalues[1]. This finding has sparked significant interest in exploring its classical counterpart across various domains, with applications in photonics[2–11], acoustics[12–21], and beyond[22–24], by utilizing balanced gain-loss regions. Anti-$\mathcal{PT}$-symmetric non-Hermitian systems, serving as the conjugate counterparts, have expanded the realm of non-Hermitian symmetries and have been experimentally realized through spatially coupled flying atom beams[25], electrical circuits[26], and optical waveguides featuring imaginary couplings[27]. Nevertheless, due to the absence of an efficient experimental methodology, the establishment of an acoustic anti-$\mathcal{PT}$-symmetric configuration remains exceedingly rare, hindering the phase transitions between $\mathcal{PT}$ and anti-$\mathcal{PT}$ symmetries within a single unified system-a challenge exacerbated by the incompatible forms of coupling leading to their anti-communication. Although studies on $\mathcal{PT}$ phase transitions, including those of anti-$\mathcal{PT}$ symmetry, in cavity-tube systems simulating tight-binding models have been reported[28], the anti-$\mathcal{PT}$ phase transitions in scattering systems remain a topic worthy of further investigation.

---

[1] School of Physics, Collaborative Innovation Center of Advanced Microstructures, Jiangsu Physical Science Research Center, Nanjing University, Nanjing, China. [2] School of Electrical and Information Engineering, Changzhou Institute of Technology, Changzhou, China. [3] National Laboratory of Solid State Microstructures, Nanjing University, Nanjing, China. [4] School of Electronic Science and Engineering, Nanjing University, Nanjing, China. [5] IMDEA Materials Institute, Getafe, Madrid, Spain. [6] These authors contributed equally: Haixiao Zhang, Renhao Fan. ✉ e-mail: chengying@nju.edu.cn; rwpeng@nju.edu.cn; liuxiaojun@nju.edu.cn; johan.christensen@imdea.org

The crucial factor in achieving the phase transition between acoustic $\mathcal{PT}$ and anti-$\mathcal{PT}$ symmetries lies in identifying dependable and controllable acoustic gain medium. While in photonics, gain can be readily induced through stimulated emission via optical or electrical excitation from an external source, or through parametric processes[29–31], the realm of acoustics faces challenges. The implementation of $\mathcal{PT}$ symmetry in experimental configurations typically necessitates the utilization of piezoelectric transducers[32], electromechanical cone loudspeakers[13,14], or forced airflows[16], as natural passive acoustic gain materials are absent. These mechanically-driven acoustic gain strategies present significant practical hurdles and impose constraints on achieving controlled $\mathcal{PT}$ symmetry due to substantial impedance mismatches with the ambient air and the inherent rigidity, leading to limited adaptability.

Nonetheless, a newer related technology, laser-induced thermoacoustics (LIT), which leverages pulsed laser light to generate acoustic waves through rapid thermal expansion may be a candidate approach for acoustic gain. This process involves three primary steps: absorption, thermal expansion, and acoustic wave generation[33]. In medical imaging, this principle is used in photoacoustic imaging, where specific wavelengths are chosen to target particular tissues or chromophores such as hemoglobin and melanin, enhancing contrast and providing detailed images of biological structures[34]. The characteristics of the generated sound waves, such as their frequency and amplitude, depend on the properties of the material and the parameters of the laser pulse, including its duration, wavelength, and intensity. This non-invasiveness is beneficial in both medical and material testing applications, where preserving the integrity of the subject is crucial. In addition, active methods for generating acoustic VB have been reported in ref. 35, and LIT may provide a viable alternative approach.

In this study, we propose a general methodology to access the complex coupling by modulating the non-Hermitian system and further facilitate the phase transitions between $\mathcal{PT}$ and anti-$\mathcal{PT}$ symmetries within a unified acoustic system using LIT. As a demonstration, we experimentally construct a compact non-Hermitian unit consisting of a pair of acoustic loss (sponge) and gain (CNT film) loaded in a waveguide. This unit provides multiple interferences in the structure when incident waves impinge on one of the components, in stark contrast to the conventional acoustic gain media like back-to-back loudspeaker pairs that absorb the incident sound field and then reradiate it[14]. Unlike $\mathcal{PT}$-symmetric system where unidirectional reflectionless can only be demonstrated from the loss side, our method reverses the orientation at identical operating frequency. Strikingly, the proposed platform also allows for the achievement of anti-$\mathcal{PT}$ symmetry through the delicate interplay between gain and loss. Due to the innovation of LIT, acoustic VBs can be conveniently generated, and their $\mathcal{PT}$-symmetric scattering behavior has been realized, along with the conversion of the topological charge. The combination of LIT and $\mathcal{PT}$-symmetric acoustics bridges two critical aspects of non-Hermitian physics, and provides diverse routes for controlling the phase transitions of non-Hermitian Hamiltonian.

Results

Non-Hermitian phase transitions with transfer matrix

The sketch, illustrating both the optical and acoustic components, is presented in Fig. 1. The optical portion illustrates the method by which the CNT film is stimulated by a 532 nm pulsed laser. The CNT film has recently emerged as a groundbreaking platform for achieving acoustic gain in a highly controllable manner[36], with significant potential for advancing acoustic devices that facilitate efficient photo-thermo-acoustic energy conversions[33,37]. Its ultrathin profile renders it acoustically transparent (Supplementary Note 1), allowing sound waves to propagate freely in the transverse direction with minimal impact on wave transmission, a feature distinct from conventional electromechanical loudspeakers that exhibit high levels of reflection. Consequently, the CNT film holds great promise for integration into acoustic non-Hermitian systems (Supplementary Note 2).

In the acoustic portion illustrated in Fig. 1, we consider a waveguide that supports plane wave propagation within the operation frequency range $k_0A < 2\pi$, where A represents the side length of the waveguide cross-section, $k_0 = \omega/c_0$ is the wave number, ω is the angular frequency, and c_0 is the sound velocity in air. By introducing a pair of loss (sponge) and gain (CNT film) material, the system becomes non-Hermitian; however, the propagation for the acoustic pressure p can still be described by the one-dimensional (1D) Helmholtz equation. We decompose the pressure field outside the photoacoustic non-Hermitian system into the forward wave (denoted by "+") and backward wave (denoted by "−"). As such, $p^+_{\mathrm{L(G)}}$ and $p^-_{\mathrm{L(G)}}$ represent the sound pressure spreading along the forward and backward directions, respectively, originating from the loss and gain sides.

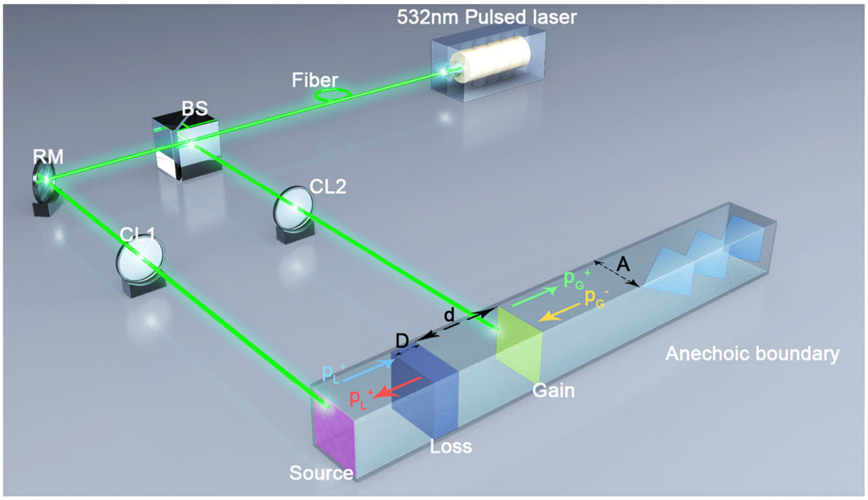

Fig. 1 | Sketch of the photoacoustic non-Hermitian system. In our experiment, the 532 nm pulsed laser is divided into two equal beams using a BS and directed onto two pieces of CNT films sequentially. BS beam splitter, RM reflector mirror, CL collimating len. At the bottom, the bianisotropic acoustic system consists of a pair of loss (porous sponge, thickness $D = 1$ cm) and gain (CNT film, thickness $h = 10$ μm) layers with coupling d. All the components are loaded in a rigid-boundary waveguide with a square cross section having side length $A = 2$ cm, ensuring 1D plane wave propagation.

The scattering matrix S_r, which describes the relationship between incoming and outgoing acoustic waves in the 1D system, can be expressed as:

$$\begin{pmatrix} p_{\mathrm{L}}^{-} \\ p_{\mathrm{G}}^{+} \end{pmatrix} = S_r \begin{pmatrix} p_{\mathrm{L}}^{+} \\ p_{\mathrm{G}}^{-} \end{pmatrix} = \begin{pmatrix} S_{11} & S_{12} \\ S_{21} & S_{22} \end{pmatrix} \begin{pmatrix} p_{\mathrm{L}}^{+} \\ p_{\mathrm{G}}^{-} \end{pmatrix}, \tag{1}$$

where S_{11} (S_{22}) represents the reflection coefficient from the loss (gain) side and S_{21} (S_{12}) represents the transmission coefficient. Due to the transmission reciprocity, we have $S_{12} = S_{21}$. S_r can be calculated using a transmission-matrix approach:

$$\begin{aligned} S_{11} &= (u\Gamma_2 + i\Lambda_2 e^{ix})/\Delta, \\ S_{22} &= (u\Gamma_1 + i\Lambda_2 e^{-ix})/\Delta, \\ S_{12} &= S_{21} = 2/\Delta, \end{aligned} \tag{2}$$

where $\Delta = -u\Gamma_1 + (2\cos y + i\Lambda_1)e^{ix}$, $x = k_0 d$, and $k_s = \omega\sqrt{\rho_s/\kappa_s}$ is the wave number in the loss medium. ρ_s and κ_s denote the mass density and bulk modulus of the loss material, respectively. Both of them can be retrieved from the experimentally measured S_r by a parameter extraction algorithm at any operating frequency[38]. The variables Γ_1, Γ_2, Λ_1, and Λ_2 are all intermediate variables with respect to coupling d. Additionally, $u = -Y_{\mathrm{CNT}}/Y_0$ denotes the complex admittance ratio between the assembled CNT film (Supplementary Note 3) and background medium air, which can be precisely adjusted by a pulsed laser. In this model, the loss medium is a conventional bulk material (porous sponge) with a defined width D, whereas the gain medium is a piece of CNT film with negligible thickness. The geometrically asymmetric unit described in Eq. (2) exhibits reciprocity and linearity, allowing different types of EPs to emerge through the tuning of coupling d (Supplementary Note 4).

For instance, $S_{11} = 0$ (the blue curve in Fig. 2) describes a reflectionless phenomenon when waves come from the loss side, which can be observed at any coupling d by adjusting the equivalent admittance ($u = -i\Lambda_2 e^{ix}/\Gamma_2$) of the assembled CNT film. Thus, the transmission evolves to $S_{21} = \Gamma_2$, and its amplitude can be modulated to 1 at a coupling of $d = 5.31$ cm with $u = 0.456 + i0.257$ [see the top maps in Fig. 2a, c]. This scattering property bears resemblance to the loss-side invisibility observed at the EP in $\mathcal{PT}$-symmetric systems. Notably, while the reflection from the gain side remains high in a $\mathcal{PT}$-symmetric system operating at this EP[14,15], the reflection from the gain side in our system is minimal [see the top map in Fig. 2b] due to the continuous interactions.

Furthermore, this setup also allows for the realization of the less commonly mentioned reversed invisibility EP in $\mathcal{PT}$-symmetric systems. Similarly, the red curve in Fig. 2 represents the reflectionless phenomenon $S_{22} = 0$ from the gain side. Thus, the admittance of the CNT film is given by $u = -i\Lambda_2 e^{-ix}/\Gamma_1$. Building upon this, the gain-side invisibility EP occurs when the amplitude of the transmission coefficient $|S_{12}| = 1/|\Gamma_1|$ equals 1 at $d = 4.34$ cm with $u = 0.435 + i0.291$ [see the middle maps in Fig. 2b, c].

Our system, by tuning the relevant parameters d and u, is also able to achieve bidirectional scattering properties at the EP of anti-$\mathcal{PT}$ symmetry, where $S_{11}^{*} = S_{22}$ and $\mathrm{Im}(S_{12}) = 0$. When focusing on the orange curve and the six bottom maps with $d = 3.88$ cm and $u = 0.657 + i0.24$ in Fig. 2, several observations can be made: first, $|S_{11}| = |S_{22}|$ in Fig. 2a, b; second, $\mathrm{Arg}(S_{11}) = -\mathrm{Arg}(S_{22})$ in Fig. 2d, e; and third, $\mathrm{Arg}(S_{12}) = 0$ in Fig. 2f. It should be noted that while we have implemented the EP of an anti-$\mathcal{PT}$-symmetric system through the intrinsic scattering matrix, our system does not need to satisfy the conditions of anti-$\mathcal{PT}$ symmetry in terms of geometry and refractive index. In addition, the phase transitions can be independently verified using a multiple-interference approach, as detailed in Supplementary Notes 5 and 6.

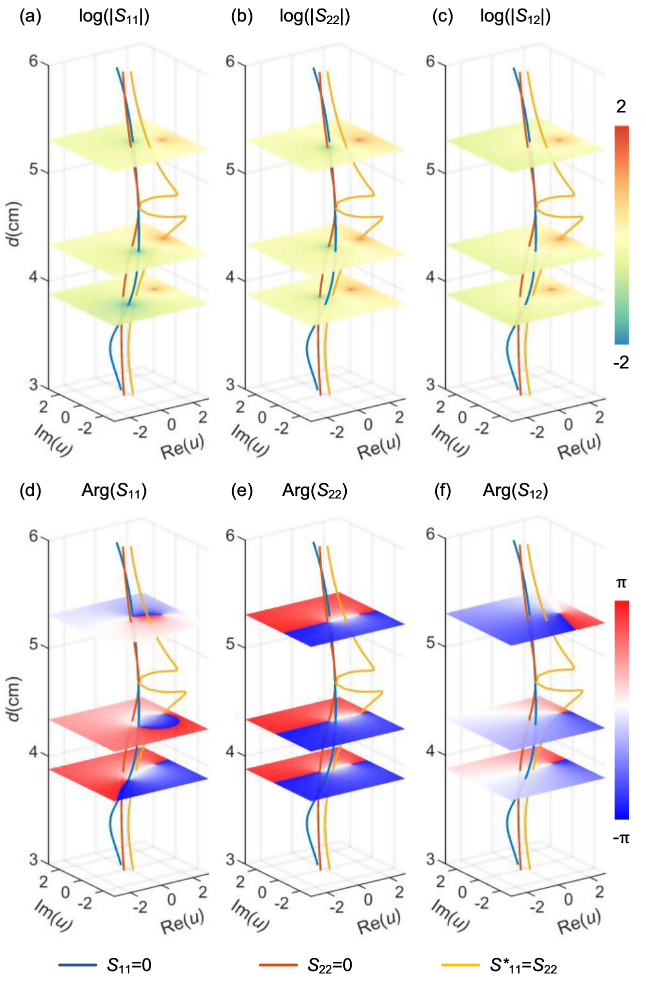

Fig. 2 | Scattering properties of the non-Hermitian system demonstrating controlled phase transitions. Logarithmic amplitudes of the reflection coefficient from the loss side (**a**), gain side (**b**), and the transmission coefficient from both sides (**c**). **d**–**f** Phases under the same conditions. The blue, red, and yellow curves represent the conditions of $S_{11} = 0$, $S_{22} = 0$, and $S_{11}^{*} = S_{22}$, respectively. The top, middle, and bottom color maps in each subgraph correspond to the phases of $\mathcal{PT}$, reversed-$\mathcal{PT}$, and anti-$\mathcal{PT}$, respectively, at the couplings of $d = 5.31$ cm, 4.34 cm and 3.88 cm.

Non-Hermitian phase transitions using LIT

In a prior study[39], we effectively showcased acoustic gain through electro-thermal-acoustic effects. Expanding on this investigation, here we present the construction of an experimental system based on LIT and establish that $\mathcal{PT}$-symmetric phase transitions can be achieved within a unified device through the manipulation of coupling d. In our configuration, the CNT film functions as a bidirectional acoustic transparent medium. This means that the change in sound pressure and medium velocity across the film is minimal, resulting in negligible impedance mismatch. Additionally, we deliberately set the specific sound pressure amplitude ratio and phase difference between the sound wave generated by the CNT film and the sound source. Consequently, the overall scattering matrix S_r can be derived as (see Supplementary Note 7 for details):

$$\begin{aligned} r_{\mathrm{L}} &= m_1 e^{i\phi_1} t_s e^{-ix} + r_s, \\ t_{\mathrm{G}} &= m_2 e^{i\phi_2} t_s e^{-ix} + t_s e^{-ix}, \\ t_{\mathrm{L}} &= m_1 e^{i\phi_1}\left(r_s e^{-i2x} + 1\right) + t_s e^{-ix}, \\ r_{\mathrm{G}} &= m_2 e^{i\phi_2}\left(r_s e^{-i2x} + 1\right) + r_s e^{-i2x}. \end{aligned} \tag{3}$$

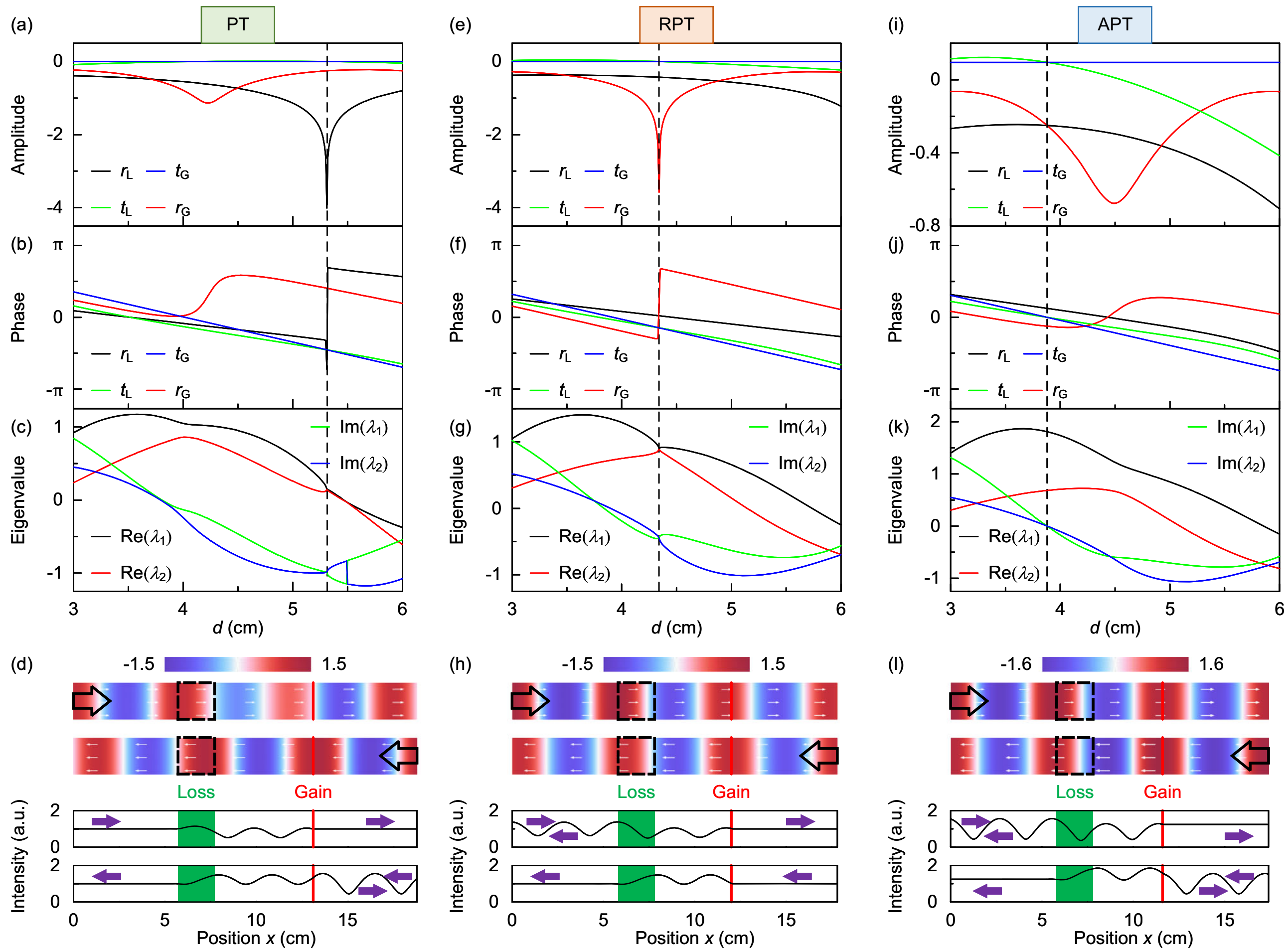

Fig. 3 | Phase transitions of the non-Hermitian system using LIT. Scattering amplitudes (**a**), phases (**b**), eigenvalues (**c**) of the $\mathcal{PT}$-symmetric EP associated with loss-side invisibility. **d** Acoustic pressure (top) and intensity (bottom) distributions at EP of loss-side from full-wave FEM simulations. The white arrows represent the direction of average power flow along the waveguide. **e**–**h** Corresponding properties of the reserved-$\mathcal{PT}$-symmetric EP for gain-side invisibility. **i**–**l** Characteristics of the anti-$\mathcal{PT}$-symmetric EP with bidirectional conjugate reflections and pure real transmission.

Here, m_1 (m_2) and ϕ_1 (ϕ_2) represent the amplitude ratio and phase difference of sound pressure between the assembled CNT film and the sound source when the incident wave comes from the loss (gain) side, respectively; r_s and t_s represent the reflection and transmission coefficients of the assembled loss material. It is worth noting that the nonreciprocal transmission phenomenon described by the 2nd and 3rd equations in Eq. (3) originates from the introduction of the CNT film, which provides abundant possibilities to manipulate the scattering properties in our configuration. In fact, our system retains sufficient degrees of freedom to convert from transmission nonreciprocity to reciprocity, and this can be achieved effectively by adjusting the geometric and laser parameters. For illustration, all controllable parameters in this study fulfill the premise of transmission reciprocity, specifically $t_L = t_G = t$. Based on this foundation, we emphasize the importance of judiciously optimizing the contrast ratio m (including m_1 and m_2), the coupling d, and ϕ (including ϕ_1 and ϕ_2) in order to attain the aforementioned three EPs in our system.

To gain a deeper understanding of these unusual scattering responses, we analyze the scattering spectra and eigenvalues of the system's scattering matrix, as shown in Fig. 3 as functions of coupling d. Figure 3a–c demonstrates the existence of an EP where loss-side invisibility occurs, characterized by parameters $m_1 = 0.262$, $\phi_1 = -0.91$, $m_2 = 0.335$, and $\phi_2 = 0.942$. At a coupling of $d = 5.31$ cm, the reflection coefficient at the loss side (r_L) is zero, indicating a sudden phase change in reflection. Meanwhile, the reflection at the gain side is nonzero with $r_G = 0.555e^{i1.237}$, which indicates the unidirectional reflectionless. This confirms that the transmission coefficients are identical in both directions ($t_L = t_G = e^{-i1.424}$) due to the system's linear time invariance and maintenance of reciprocity. The theoretical analysis of scattering coefficients, in which the CNT film parameters vary as functions of the coupling d have been demonstrated in Supplementary Note 8, confirming the identical positions of the EPs coincide precisely. To further validate the EP nature of this operation point, we calculate the eigenvalues of the S_t matrix using

$$S_t = S_r\sigma_x = \begin{pmatrix} r_L & t_G \\ t_L & r_G \end{pmatrix}\begin{pmatrix} 0 & 1 \\ 1 & 0 \end{pmatrix} = \begin{pmatrix} t_G & r_L \\ r_G & t_L \end{pmatrix}, \tag{4}$$

where σ_x represents one of the Pauli matrices. The eigenvalues of the S_t matrix can be expressed as

$$\lambda_{1,2} = \frac{t_L + t_G}{2} \pm \sqrt{r_L t_G + \left(\frac{t_L - t_G}{2}\right)^2}. \tag{5}$$

As can be seen from Fig. 3c, at coupling $d = 5.31$ cm, there is a coalescence of the real part of the eigenvalues, and the imaginary part experiences biased distributions when $d > 5.31$ cm. Such eigenvalue spectrum is the characteristic behavior of a $\mathcal{PT}$-symmetric system that is experiencing a transition from $\mathcal{PT}$-exact phase to $\mathcal{PT}$-broken phase at the EP.

Full-wave simulations are performed with the finite element solver COMSOL Multiphysics, thus the acoustic pressure and intensity distributions are shown in Fig. 3d. It can be seen that for incoming waves in opposite directions, the reflected pressure fields display vastly different characteristics at the designed operational distance. The reflection at the loss side is almost zero, while the acoustic pressure distributions on the transmission are identical in terms of amplitude and phase since the system has been regulated reciprocity.

Likewise, Fig. 3e–h illustrates the EP of gain-side invisibility with parameters m_1 = 0.262, ϕ_1 = 0.128, m_2 = 0.262, and ϕ_2 = 0.589 at a coupling of d = 4.34 cm. Evidently, a reflectionless phenomenon is observed from the gain side ($r_G = 0$), while the reflection from the loss side is also present at a lower level ($r_L = 0.37e^{i0.067}$). These amplitude and phase behaviors are typical of the scattering matrix and eigenvalues of a $\mathcal{PT}$-symmetric system, as shown in Fig. 3g, h.

As anticipated, the scattering behavior at the EP of an anti-$\mathcal{PT}$-symmetric system differs significantly from that at the EP of a $\mathcal{PT}$-symmetric system. The laser parameters for this EP are $m_1 = 0.436$, ϕ_1 = 0.349, m_2 = 0.537, and ϕ_2 = 0.21 at a coupling of d = 3.88 cm. Figure 3i–l illustrates the presence of conjugated reflections ($r_L = 0.562e^{i0.391}$ and $r_G = 0.562e^{-i0.391}$) from both sides, as well as bidirectional transmission ($t_L = t_G = 1.246$). It should be noted that at the EP, the eigenvalues can be expressed as $\lambda_{1,2} = t \pm \sqrt{r_L r_G}$, where $t_L = t_G = t$. Consequently, the eigenvalues become two unequal real numbers, as depicted in Fig. 3k, confirming the true nature of this EP as an anti-$\mathcal{PT}$-symmetric system. By the way, the corresponding pressure and intensity distributions at the EP are shown in Fig. 3l.

Experimental demonstration

The excellent agreement between analytical and full-wave simulation results is further validated by the experimental measurements (Supplementary Note 14). Figure 4a shows the measured scattering amplitude spectra of the LIT system in the loss and gain directions. When all the parameters for the experiment of $\mathcal{PT}$-symmetric EP of loss-side invisibility were configured, we observed 3.5% reflection from the loss side and a reflection of about 55.3% from the gain side, which can verified by examining the phase spectra in Fig. 4b.

Furthermore, we observed almost total transmission with $t_L = 0.993e^{-i1.428}$ and $t_G = 0.994e^{-i1.442}$. A similar result about the reversed-$\mathcal{PT}$ symmetry of gain-side invisibility can be obtained from Fig. 4c, d. The measured scattering matrix is r_L = $0.382e^{i0.052}$, t_L = $0.996e^{-i0.461}$, r_G = $0.031e^{i0.52}$, and t_G = $1.003e^{-i0.466}$, indicating distinctly different reflection characteristics in opposite directions and highlighting the unidirectional scattering properties of the photoacoustic non-Hermitian bianisotropic system.

On the other hand, the experimental results demonstrating the anti-$\mathcal{PT}$-symmetric EP of bidirectional conjugated reflections and pure real transmission are shown in Fig. 4e, f. Consistent with the simulation curves, both the bidirectional reflection amplitudes and transmission amplitudes intersect at f_0 = 6 kHz in Fig. 4e. Additionally, the bidirectional reflection phases are opposite to each other, while the transmission phases are close to 0 in Fig. 4f. More specifically, the measured scattering matrix at the EP is r_L = $0.578e^{i0.401}$, t_L = $1.256e^{-i0.02}$, $r_G = 0.567e^{-i0.405}$, and $t_G = 1.239e^{-i0.01}$, illustrating the EP behavior of the anti-$\mathcal{PT}$-symmetric system.

Formation of acoustic VBs and scattering EP using LIT

The LIT method employed in this study represents a promising approach for achieving perfect acoustic VBs and enables the $\mathcal{PT}$-symmetric scattering behavior illustrated in Fig. 5a. In the aforementioned configuration, the CNT film under laser irradiation functions effectively as a point sound source, since the timescale of laser-induced heat diffusion across the film surface is on the order of seconds[40]. When the laser spot rotates on the CNT film at a modulation frequency of f_r (e.g., f_r = 0.1 kHz), the diffusion time is much longer than the rotation period, ensuring that the acoustic source rotates continuously rather than discretely. As a result, the system produces perfect acoustic VBs within the waveguide, unlike the approximate VBs generated by discrete passive[41] or electronical driven[35] methods. This continuous, contact-free excitation is a defining advantage of LIT and fundamentally differentiates it from previous electrical approaches.

The physical mechanism and spatial distribution of the acoustic VB generated by a rotating laser spot are discussed in Supplementary Note 10. To support the propagation of first-order VBs, the waveguide was replaced with a cylindrical tube of radius R_0 = 2 cm. A schematic of the LIT-generated VB is shown in Fig. 5b, in which a certain angle is set between the symmetry axis of the reflector and the rotation axis of the motor, causing the laser to trace a circular trajectory on the CNT film. Supplementary Movies 1 and 2 demonstrate the laser spot rotating on the CNT film to form a circular trajectory at rotational speeds of 150 revolutions per minute (RPM) and 6000 RPM, respectively. The corresponding simulation and experimental results, after Fourier

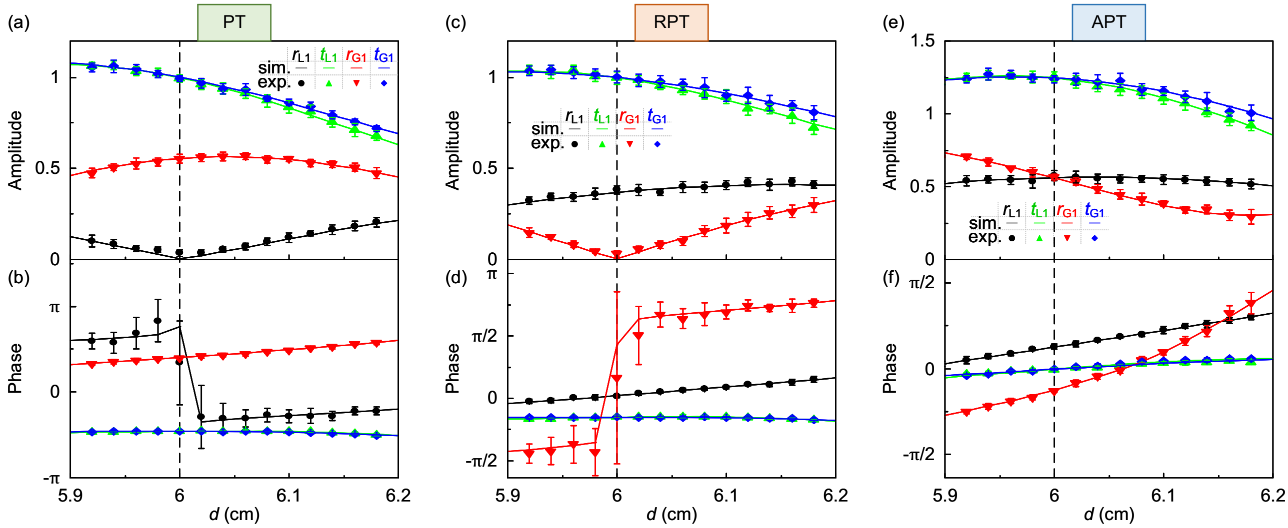

Fig. 4 | Experimental demonstration of the three idiosyncratic EPs in the non-Hermitian system using LIT. a, b Simulated (curves) and experimentally measured (icons) amplitudes and phases of $\mathcal{PT}$ symmetry with coupling d = 5.31 cm, respectively. **c**, **d** Same as (**a**, **b**), but for the reserved-$\mathcal{PT}$ symmetry with coupling d = 4.34 cm. **e**, **f** Same as (**a**, **b**), but for the anti-$\mathcal{PT}$ symmetry with coupling d = 3.88 cm. Error bars correspond to the standard deviation (s.d.) of a collection of ten measurements.

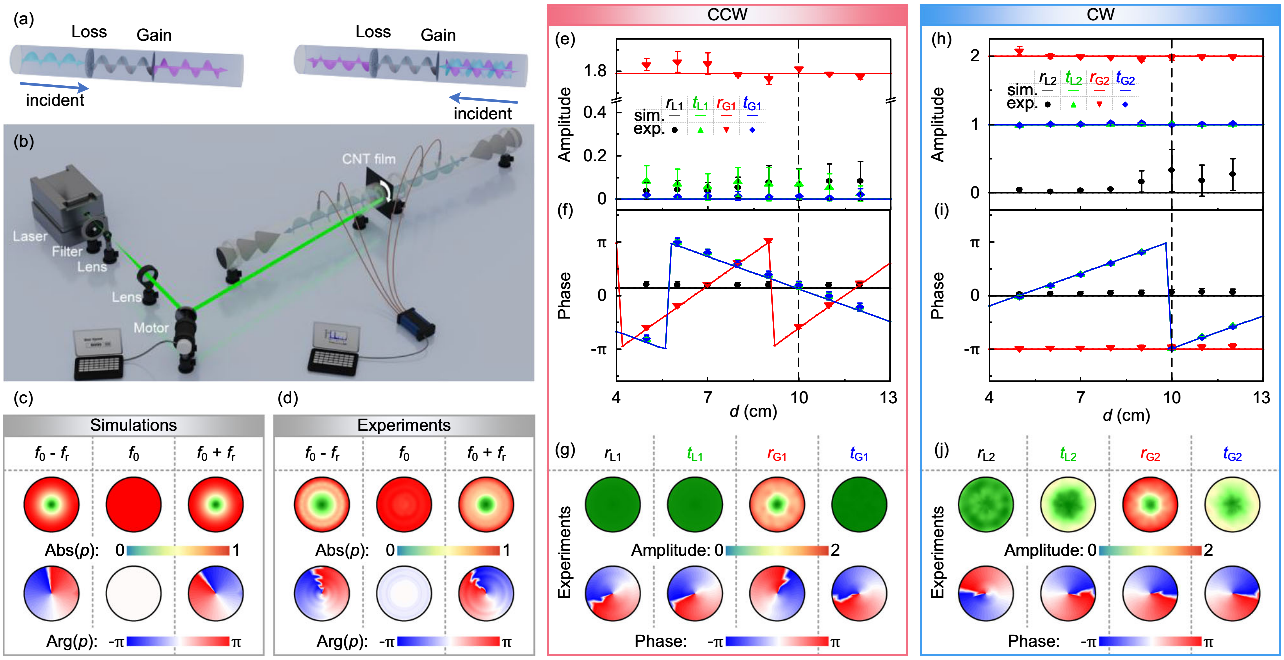

Fig. 5 | Formation of acoustic VBs and realization of the scattering EP using LIT. **a** Illustration of the $\mathcal{PT}$-symmetric system for acoustic VBs. **b** Schematic of the LIT-based generation of acoustic VBs. **c**, **d** Simulated and experimental demonstration of the acoustic VBs by CCW-rotating lasr spot. **e**, **f** Simulated (curves) and experimentally measured (symbols) scattering amplitudes and phases of CCW VBs at a rotation frequency of f_r = 0.1 kHz. **g** Measured scattering field amplitudes and phases of CCW VBs with a coupling of d = 9.92 cm, corresponding to the data in (**e**, **f**). **h**, **i** Same as (**e**, **f**), but for CW VBs, obtained under identical conditions. **j** Same as (**g**), but for CW VBs, corresponding to (**h**, **i**). Error bars in (**e**, **f**) and (**h**, **i**) correspond to the standard deviation (s.d.) of a collection of five measurements.

transformation, are presented in Fig. 5c, d, confirming that the LIT system produces a stable and well-defined acoustic VB (details in Supplementary Note 11).

Building on this foundation, we modeled the quasi-$\mathcal{PT}$-symmetric scattering behavior of VBs at the EP and verified the results experimentally. The scattering responses for counter-clockwise (CCW) vortex excitations were formulated (see Supplementary Note 12), with the corresponding scattering matrices revealing distinct symmetry-breaking features inherent to non-Hermitian systems:

$$S_r = \begin{bmatrix} r_L & t_G \\ t_L & r_G \end{bmatrix} = \begin{bmatrix} r_{L1} & t_{G1} \\ t_{L1} & r_{G1} \end{bmatrix}_{CCW} + \begin{bmatrix} r_{L2} & t_{G2} \\ t_{L2} & r_{G2} \end{bmatrix}_{CW}, \tag{6}$$

in which

$$\begin{aligned} r_{L1} &= m_{11}e^{i\phi_{11}}t_s e^{-iy} + r_s, \\ t_{G1} &= m_{21}e^{i\phi_{21}}t_s e^{-iy} + t_s e^{-iy}, \\ t_{L1} &= m_{11}e^{i\phi_{11}}r_s e^{-i2y} + m_{12}e^{i\phi_{12}} + t_s e^{-iy}, \\ r_{G1} &= m_{21}e^{i\phi_{21}}r_s e^{-i2y} + m_{22}e^{i\phi_{22}} + r_s e^{-i2y}, \end{aligned} \tag{7}$$

and

$$\begin{aligned} r_{L2} &= m_{12}e^{i\phi_{12}}t_s e^{-iy}, \\ t_{G2} &= m_{22}e^{i\phi_{22}}t_s e^{-iy}, \\ t_{L2} &= m_{11}e^{i\phi_{11}} + m_{12}e^{i\phi_{12}}r_s e^{-i2y}, \\ r_{G2} &= m_{21}e^{i\phi_{21}} + m_{22}e^{i\phi_{22}}r_s e^{-i2y}. \end{aligned} \tag{8}$$

The parameters r_{L1}, t_{G1}, t_{L1}, r_{G1} describe the CCW VB relative to the incident wave at an azimuthal angle of $\theta = 0$, meanwhile r_{L2}, t_{G2}, t_{L2}, r_{G2} characterize the clockwise (CW) VB response. Here, the frequencies of the VBs are all given by $f = f_0 + f_r$. m_{ij} and ϕ_{ij} represent the amplitude ratios and phase differences between the CNT film components excited by CW ($j = 1$) and CCW ($j = 2$) rotating laser spots and the incident CCW VB coming from the loss ($i = 1$) and gain ($i = 2$) sides, respectively. The propagation constant is expressed as $k_x^{11} = \sqrt{(\omega/c_0)^2 - (k_r^{11})^2}$ with $y = k_x^{11}d$, in which k_r^{11} is the first order radial wave number of the waveguide. It is worth emphasizing that the scattering coefficients represent only the normalized ratios between the reflected or transmitted pressure amplitudes and that of the incident wave. These quantities are independent of the vortex topological charge itself; the charge merely determines the rotational phase structure of the field.

Figure 5e, f demonstrated the simulated and experimentally measured scattering amplitudes and phases of the acoustic CCW VBs at the operating frequency of f_0 = 6 kHz and rotation frequency of f_r = 0.1 kHz, respectively. The corresponding CW characteristics are shown in Fig. 5h, i. The data reveal a remarkable behavior: when a CCW VB is incident from the lossy side, no reflection occurs ($r_L = 0$), and the transmitted beam takes the form $t_L = -e^{iy}$. The transmitted VB preserves its amplitude but reverses its topological charge relative to the incident wave. In contrast, when the VB is incident from the gain side, the transmitted mode remains reversed ($t_G = -e^{iy}$), while the reflected field becomes a superposition of two VBs with distinct topological charges, $r_G = r_{G1} + r_{G2} = -e^{i2y}/s - 2$ (see Supplementary Note 13 for details). Here, s is the complex reflection/transmission coefficient of the loss medium with $r_s = t_s = s = |s|e^{i\alpha}$; $|s|$ and α are the amplitude and phase of s.

A more intuitive visualization is provided in Fig. 5g, j, showing the measured cross-sectional field distributions of CCW and CW VBs with a coupling d = 9.92 cm, corresponding to the vertical dashed lines in Fig. 5**e**, **f**, **h**, **i**, respectively. The fitted CNT film parameters for this EP are $m_{11} = 1$, $\phi_{11} = \pi$; $m_{12} = 0$, $\phi_{12} = 0$; $m_{21} = 1$, $\phi_{21} = \pi$; and $m_{22} = 1/|s|$, $\phi_{22} = \pi - \alpha$. The experimentally obtained scattering coefficients are $r_{L1} = 0.068e^{i0.619}$, $t_{L1} = 0.069e^{i0.57}$, $r_{G1} = 1.811e^{-i1.803}$, $t_{G1} = 0.015e^{i0.615}$,

$r_{L2} = 0.327e^{i0.181}$, $t_{L2} = 1.016e^{-i3.102}$, $r_{G2} = 1.982e^{-i3.015}$, and $t_{G2} = 0.997e^{-i3.1}$ at the azimuth angle of $\theta = 0$. These results collectively confirm the realization of $\mathcal{PT}$-symmetric scattering with acoustic VBs and the experimental observation of topological charge reversal at the EP. This finding represents the first experimental demonstration of $\mathcal{PT}$ symmetry in acoustic VBs, marking a substantial advance in non-Hermitian acoustics. The LIT platform not only enables the study of symmetry breaking in structured acoustic fields but also establishes a versatile route for exploring topological effects and non-Hermitian phase transitions beyond plane-wave systems.

Discussion

To summarize, we have theoretically proposed and experimentally demonstrated an effective route to construct acoustic controlled non-Hermitian system based on LIT of a laser-pumped CNT film. This approach allows for the distinct observation of the phase transitions between $\mathcal{PT}$- and anti-$\mathcal{PT}$-symmetric acoustics within a unified unit. The introduction of the CNT film leads to intricate interferences between the control sound source and the stimulated components, enabling seamless transformation between dissipative and $\mathcal{PT}$-symmetric systems. Importantly, all of these phenomena can be achieved by precisely optimizing the relevant parameters over a broad frequency range (Supplementary Note 9), regardless of the dispersion properties of the loss material. The realization of $\mathcal{PT}$-symmetric scattering behavior in acoustic VBs marks a key step forward in extending $\mathcal{PT}$ symmetry from plane-wave systems to structured wavefronts carrying orbital angular momentum. In addition, from a device perspective, the CNT film is highly flexible and stretchable, allowing for the fabrication of structures in 1D, 2D, and 3D configurations. This opens up possibilities for experimental realization of high-order non-Hermitian $\mathcal{PT}$-symmetric systems and topological acoustic systems, which cannot be achieved using electromechanical loudspeakers or other acoustic gain elements[42]. Moreover, the proposed manipulation strategy can also be extended to non-Hermitian systems without $\mathcal{PT}$ symmetry or $\mathcal{PT}$-symmetric periodic superlattices[30]. It is worth noting that recent advancements in time-variant metamaterials[43] offer a new perspective on our presented system, where the impedance of the CNT film with LIT varies over time. Last but not least, this ability to intentionally control sound propagation provides a fertile ground for developing asymmetric wave propagation physics and holds promising applications for non-Hermitian acoustic devices.

Methods

Loss measurement

In order to verify the universality of this methodology, a common sponge sheet was selected as the acoustic loss material in our experiments. In the plane wave scenario, the measured reflection and transmission coefficients of the loss at 6 kHz are $r_s = 0.213e^{i0.585}$ and $t_s = 0.815e^{-i2.093}$. A standard extraction algorithm is used to retrieve the effective parameters of the sponge from the measured scattering matrix[38]. In our prototype sample, the mass density of surrounding background medium (air) is $\rho_0 = 1.21\,\mathrm{kg/m^3}$ and the bulk modulus is $\kappa_0 = 0.142$ MPa. Thus, the retrieved mass density and bulk modulus are $\rho_s = 1.339e^{i0.144}\,\mathrm{kg/m^3}$ and $\kappa_s = 0.177e^{i0.342}$ MPa, respectively. On the other hand, in the acoustic VB scenario, the reflection and transmission coefficients of the loss (thickness $D = 0.4$ cm) at 6.1 kHz are $r_s = t_s = 0.559e^{-i1.137}$, and the retrieved mass density and bulk modulus are $\rho_s = 2.236e^{-i.249}\,\mathrm{kg/m^3}$ and $\kappa_s = 0.12e^{-i0.444}$ MPa, respectively.

Active gain design

A CNT film irradiated by pulsed laser is used to achieve an artificial acoustic gain material since no passive acoustic gain material exists in nature. The film is placed inside the waveguide vertically and hence radiates plane waves (or VBs) facing opposite directions with identical amplitude and initial phase when pumped by laser. We control the effective transmission and reflection of the artificial CNT film to generate the predesigned effective gain medium.

Full-wave simulations

The simulations are performed by the full-wave finite element solver COMSOL Multiphysics, through which we validate these unusual scattering responses and obtain in-depth physical insights into the operation of this device. The pressure acoustic module and the acoustic heat source domain are used so that both loss and CNT can be fully modeled for this multi-physics process. The calculation domain is terminated by radiation boundary conditions that also include the incident field.

Data availability

All technical details for producing the figures are enclosed in the manuscript and the Supplementary Information. Data are available from the corresponding authors upon request.

Code availability

All technical details for implementing the simulations are enclosed in the manuscript and the Supplementary Information. Codes are available from the corresponding authors upon request.

References

1. Bender, C. M. & Boettcher, S. Real spectra in non-Hermitian hamiltonians having $\mathcal{PT}$ symmetry. *Phys. Rev. Lett.* **80**, 5243 (1998).
2. Rüter, C. E. et al. Observation of parity–time symmetry in optics. *Nat. Phys.* **6**, 192–195 (2010).
3. Lin, Z. et al. Unidirectional invisibility induced by $\mathcal{PT}$-symmetric periodic structures. *Phys. Rev. Lett.* **106**, 213901 (2011).
4. Feng, L. et al. Experimental demonstration of a unidirectional reflectionless parity-time metamaterial at optical frequencies. *Nat. Mater.* **12**, 108–113 (2013).
5. Fleury, R., Sounas, D. L. & Alù, A. Negative refraction and planar focusing based on parity-time symmetric metasurfaces. *Phys. Rev. Lett.* **113**, 023903 (2014).
6. Monticone, F., Valagiannopoulos, C. A. & Alù, A. Parity-time symmetric nonlocal metasurfaces: all-angle negative refraction and volumetric imaging. *Phys. Rev. X* **6**, 041018 (2016).
7. Wong, Z. J. et al. Lasing and anti-lasing in a single cavity. *Nat. Photonics* **10**, 796–801 (2016).
8. Feng, L., El-Ganainy, R. & Ge, L. Non-hermitian photonics based on parity-time symmetry. *Nat. Photonics* **11**, 752–762 (2017).
9. Liu, Y. et al. Observation of parity-time symmetry in microwave photonics. *Light Sci. Appl.* **7**, 38 (2018).
10. Luo, J., Li, J. & Lai, Y. Electromagnetic impurity-immunity induced by parity-time symmetry. *Phys. Rev. X* **8**, 031035 (2018).
11. Wang, C., Sweeney, W. R., Stone, A. D. & Yang, L. Coherent perfect absorption at an exceptional point. *Science* **373**, 1261–1265 (2021).
12. Zhu, X., Ramezani, H., Shi, C., Zhu, J. & Zhang, X. $\mathcal{PT}$-symmetric acoustics. *Phys. Rev. X* **4**, 031042 (2014).
13. Fleury, R., Sounas, D. L. & Alù, A. An invisible acoustic sensor based on parity-time symmetry. *Nat.Commun.* **6**, 5905 (2015).
14. Shi, C. et al. Accessing the exceptional points of parity-time symmetric acoustics. *Nat. Commun.* **7**, 11110 (2016).
15. Christensen, J., Willatzen, M., Velasco, V. & Lu, M. Parity-time synthetic phononic media. *Phys. Rev. Lett.* **116**, 207601 (2016).
16. Aurégan, Y. & Pagneux, V. $\mathcal{PT}$-symmetric scattering in flow duct acoustics. *Phys. Rev. Lett.* **118**, 174301 (2017).
17. Rivet, E. et al. Constant-pressure sound waves in non-Hermitian disordered media. *Nat. Phys.* **14**, 942–947 (2018).
18. Shen, C., Li, J., Peng, X. & Cummer, S. A. Synthetic exceptional points and unidirectional zero reflection in non-hermitian acoustic systems. *Phys. Rev. Mater.* **2**, 125203 (2018).

19. Liu, T., Zhu, X., Chen, F., Liang, S. & Zhu, J. Unidirectional wave vector manipulation in two-dimensional space with an all passive acoustic parity-time-symmetric metamaterials crystal. *Phys. Rev. Lett.* **120**, 124502 (2018).
20. Zhang, H., Zhang, Y., Liu, X., Bao, Y. & Zhao, J. Acoustic impurity shielding induced by a pair of metasurfaces respecting $\mathcal{PT}$ symmetry. *Phys. Rev. B* **106**, 094101 (2022).
21. Zhang, H., Hu, B., Xiong, W., Cheng, Y. & Liu, X. Manipulation of invisible cloaking in $\mathcal{PT}$-symmetric thermoacoustic dimer. *Sci. China Phys. Mech. Astron.* **66**, 124312 (2023).
22. Schindler, J., Li, A., Zheng, M. C., Ellis, F. M. & Kottos, T. Experimental study of active LRC circuits with $\mathcal{PT}$ symmetries. *Phys. Rev. A* **84**, 040101 (2011).
23. Xiao, Z., Ra'di, Y., Tretyakov, S. & Alù, A. Microwave tunneling and robust information transfer based on parity-time-symmetric absorber-emitter pairs. *Research* **2019**, 7108494 (2019).
24. Li, Y. et al. Anti–parity-time symmetry in diffusive systems. *Science* **364**, 170–173 (2019).
25. Peng, P. et al. Anti-parity-time symmetry with flying atoms. *Nat. Phys.* **12**, 1139–1145 (2016).
26. Choi, Y., Hahn, C., Yoon, J. W. & Song, S. H. Observation of an anti-$\mathcal{PT}$-symmetric exceptional point and energy-difference conserving dynamics in electrical circuit resonators. *Nat. Commun.* **9**, 2182 (2018).
27. Ge, L. & Türeci, H. E. Antisymmetricpt-photonic structures with balanced positive- and negative-index materials. *Phys. Rev. A* **88**, 1094–1622 (2013).
28. Hu, B. et al. Anti-parity-time symmetry in a su-schrieffer-heeger sonic lattice. *Phys. Rev. Lett.* **131**, 066601 (2023).
29. Ganainy, R. E. et al. Non-hermitian physics and $\mathcal{PT}$ symmetry. *Nat. Phys.* **14**, 11–19 (2018).
30. Özdemir, Ş, Rotter, S., Nori, F. & Yang, L. Parity-time symmetry and exceptional points in photonics. *Nat. Mater.* **18**, 783–798 (2019).
31. Klauck, F. et al. Observation of $\mathcal{PT}$-symmetric quantum interference. *Nat. Photonics* **13**, 883–887 (2019).
32. Suzuki, K. et al. Study of carbon-nanotube web thermoacoustic loud speakers. *Jpn. J. Appl. Phys.* **50**, 01BJ10 (2011).
33. Tian, Y. et al. Coherent generation of photo-thermo-acoustic wave from graphene sheets. *Sci. Rep.* **5**, 10582 (2015).
34. Wang, L. V. & Yao, J. A practical guide to photoacoustic tomography in the life sciences. *Nat. Methods* **13**, 627–638 (2016).
35. Jia, Y. et al. Orbital angular momentum multiplexing in space-time thermoacoustic metasurfaces. *Adv. Mater.* **34**, 2202026 (2022).
36. Lim, C., Tong, L. & Li, Y. Theory of suspended carbon nanotube thinfilm as a thermal-acoustic source. *J. Sound Vib.* **332**, 5451–5461 (2013).
37. Giorgianni, F. et al. High-efficiency and low distortion photo-acoustic effect in 3D graphene sponge. *Adv. Funct. Mater.* **28**, 1702652 (2018).
38. Fokin, V., Ambati, M., Sun, C. & Zhang, X. Method for retrieving effective properties of locally resonant acoustic metamaterials. *Phys. Rev. B* **76**, 144302 (2007).
39. Hu, B. et al. Non-hermitian topological whispering gallery. *Nature* **597**, 655–659 (2021).
40. Balandin, A. A. Thermal properties of graphene and nanostructured carbon materials. *Nat. Mater.* **10**, 569–581 (2011).
41. Jiang, X., Li, Y., Liang, B., Cheng, J.-C. & Zhang, L. Convert acoustic resonances to orbital angular momentum. *Phys. Rev. Lett.* **117**, 034301 (2016).
42. Nejad, F. Z. & Fleury, R. Active times for acoustic metamaterials. *Rev. Phys.* **4**, 100031 (2019).
43. Bacot, V., Labousse, M., Eddi, A., Fink, M. & Fort, E. Time reversal and holography with spacetime transformations. *Nat. Phys.* **12**, 972–977 (2016).

Acknowledgements

This work was supported by the National Key R&D Program of China (2022YFA1404400), the National Natural Science Foundation of China (12474448, 12225408, 12074183, 11904035, and 12227809), the China Postdoctoral Science Foundation (2024M751371), the Natural Science Foundation of Jiangsu Province (BK20241774), the Qing Lan Project of Jiangsu Province, Young Elite Scientists Sponsorship Program by Jiangsu Province (JSTJ-2024-143) and the Natural Science Foundation of the Jiangsu Higher Education Institutions of China (23KJD140001). R.P. acknowledges support from the National Key R&D Program of China (2022YFA1404303), the National Natural Science Foundation of China (12234010), and the Natural Science Foundation of Jiangsu Province (BK20233001). J.C. acknowledges support from the Spanish Ministry of Science and Innovation through a Consolidación Investigadora grant (CNS2022-135706).

Author contributions

H.Z. and Y.C. conceived the idea and initiated the project. Y.C., R.P., X.L., and J.C. guided the research. H.Z., R.F,. and W.X. carried out the theoretical analyses and conducted FEM simulations. H.Z., R.F., W.X., K.S., A.Z., Z.Z., C.S., C.M., and Y.B. designed the experimental setup and conducted the measurements. H.Z., Y.C., and J.C. wrote the manuscript. All authors contributed to the discussions of the results and the manuscript preparation. H.Z. and R.F. contributed equally to this work.

Competing interests

The authors declare no competing interests.

Additional information

Supplementary information The online version contains supplementary material available at https://doi.org/10.1038/s41467-026-69986-w.

Correspondence and requests for materials should be addressed to Ying Cheng, Ruwen Peng, Xiaojun Liu or Johan Christensen.

Peer review information *Nature Communications* thanks the anonymous reviewers for their contribution to the peer review of this work. A peer review file is available.